Carbon 143 (2019) 531–541

Contents lists available at ScienceDirect

Carbon

journal homepage: www.elsevier.com/locate/carbon

In-situ ion-activated carbon nanospheres with tunable ultramicroporosity for superior CO_2 capture

Zhen Zhang [a, b, 1], Dan Luo [a, 1], Gregory Lui [a], Gaoran Li [a], Gaopeng Jiang [a], Zachary Paul Cano [a], Ya-Ping Deng [a], Xiaojuan Du [c], Song Yin [d], Yifei Chen [d], Minhua Zhang [d, ***], Zifeng Yan [b, **], Zhongwei Chen [a, *]

[a] Department of Chemical Engineering, University of Waterloo, Waterloo, Ontario, N2L 3G1, Canada
[b] State Key Laboratory of Heavy Oil Processing, PetroChina Key Laboratory of Catalysis, China University of Petroleum, Qingdao, 266580, China
[c] College of Petroleum Engineering, State Key Laboratory of Heavy Oil Processing, China University of Petroleum, Qingdao, 266580, China
[d] Key Laboratory for Green Chemical Technology of Ministry of Education, R&D Center for Petrochemical Technology, Tianjin University, Tianjin, 300072, China

ARTICLE INFO

Article history:
Received 26 September 2018
Received in revised form
30 October 2018
Accepted 31 October 2018
Available online 1 November 2018

ABSTRACT

Ultramicroporous carbon materials play a critical role in CO_2 capture and separation, however facile approaches to design ultramicroporous carbon with controllable amount, ratio and size of pores are still challenging. Herein, a novel strategy to design carbon nanospheres with abundant, uniform, and tunable ultramicroporosity was developed based on an in-situ ionic activation methodology. The adjustable ion-exchange capacity derived from oxidative functionalization was found capable of substantially governing the ionic activation and precisely regulating the ultramicroporosity in the resultant product. An ultrahigh ultramicropore content of 95.5% was achieved for the optimally-designed carbon nanospheres, which demonstrated excellent CO_2 capture performances with extremely high capacities of 1.58 mmol g^{-1} at typical flue gas conditions and 4.30 mmol g^{-1} at 25 °C and ambient pressure. Beyond that, the CO_2 adsorption mechanism in ultramicropore was also investigated through molecular dynamics simulation to guide the pore size optimization. This work provides a novel and facile guideline to engineer carbon materials with abundant and tunable ultramicroporosity towards superior CO_2 capture performance, which also delivers great potential in extensive applications such as water purification, catalysis, and energy storage.

1. Introduction

The contribution of increasing concentration of atmospheric carbon dioxide (CO_2) to climate change has caused significant public concerns over the last few decades [1,2]. According to the recent report "Global Carbon Budget", the global CO_2 emission reached a record high of 40.6 billion tonnes in 2016 [3]. Despite critical warnings about the necessity to restrain greenhouse gases, a 2.0% increase in CO_2 discharge is estimated over 2017. The search for improved or alternative methods to capture released CO_2 has been stimulating tremendous research enthusiasm in academia and industry [4–6]. In recent years, various technologies have been developed for CO_2 capture such as adsorption by porous solids [7], absorption by amine-based materials [8] and membrane separation [9]. Among them, adsorption using porous carbon is deemed as one of the most promising technologies employed in a wide range of operating conditions, due to its good chemical resistance to both alkaline and acidic media, excellent thermal stability, and easily fast regeneration [10,11]. The CO_2 adsorption capacity at ambient pressure recently has been recognized to be mainly determined by the volume of ultramicropores (diameter < 0.7 nm) instead of the specific surface area and total pore volume [12–14]. The CO_2 adsorption is subject to the ultramicropores smaller than a certain pore width at different temperatures and pressures. Ultramicroporous carbon exhibits exquisite pore structure, which is able

* Corresponding author.
** Corresponding author.
*** Corresponding author.
E-mail addresses: mhzhang@tju.edu.cn (M. Zhang), zfyancat@upc.edu.cn (Z. Yan), zhwchen@uwaterloo.ca (Z. Chen).
[1] These authors contributed equally to this work.

https://doi.org/10.1016/j.carbon.2018.10.096
0008-6223/

to trap the CO_2 molecules efficiently with a high adsorption capability [15]. Therefore, rational design and regulation of ultramicroporosity in carbon materials is of crucial importance for high-efficiency CO_2 capture.

During the past few decades, various synthetic strategies have been developed for porous carbon materials, including physical activation [16,17], chemical activation [18–20], and template methods [21,22]. However, these conventional strategies usually deliver poor control over the ultramicroporous structure as well as an unsatisfactory ultramicropore content in the products. For instance, the most widely-used chemical activation is employing alkalis (e.g. KOH or K_2CO_3) as activation agents via simply physical mixing [23–25]. However, the large amount of alkalis in these inhomogeneous mixtures are prone to damaging the structure and morphology of the product carbon materials, leading to non-uniform dispersion and low fractions of ultramicropores. Moreover, the large use of strong alkalis triggers a corrosive, costly, and risky synthetic process, which is adverse to large-scale and sustainable fabrication. As such, the development of facile and green strategies to construct as well as finely tuning the ultramicroporous features in carbon materials is still challenging but of great significance for efficient CO_2 capture.

Herein, we developed a new strategy based on the ionic activation to facilely and precisely tune the ultramicroporosity of carbon materials. The synthetic process involves sequentially the hydrothermal treatment, oxidative calcination, ion exchange, and pyrolytic etching process. The obtained carbon nanospheres were endowed with an ultrahigh content of ultramicropores and uniform pore distribution, which were employed as the effective adsorbent for CO_2 capture. This synthetic design delivers several apparent advantages: 1) a low-concentration KOH solution was employed for the ion exchange with carboxyl to form the in-situ immobilized potassium ions, which serve as the activating agents in the final pyrolytic etching process. This not only favors the efficient and homogeneous ultramicropore formation, but also circumvents the use of corrosive alkali activating agents for the improved eco-benignity; 2) more importantly, the ultramicroporosity in the product carbon nanospheres can be facilely and finely tuned by adjusting the ion-exchange capacity in the oxidative treatment process; 3) the well optimized synthesis enables a high ion-exchange capacity of 3.92 mmol g^{-1}, which contributes to a high yield of ultramicropores up to 95.5% in the final product. The as-developed carbon nanospheres show the excellent CO_2 capture performance with an ultrahigh capacity of 1.58 mmol g^{-1} at the typical flue gas condition and 4.30 mmol g^{-1} at 25 °C and ambient pressure. To the best of our knowledge, these values are higher than most of the reported carbon materials, including numerous N-doped carbons. The adsorption mechanism and optimal pore width for CO_2 adsorption are also investigated by theoretical calculations based on the grand canonical Monte Carlo (GCMC) simulations, which predict the thermodynamic equilibrium properties of the CO_2-carbon pore system. This strategy offers a novel and facile guideline from adjusting ion-exchange capacity to tuning ultramicroporosity for carbon materials, holding great potential to meet the extensive structural demands in gas adsorption and separation, as well as other related areas.

2. Experimental

2.1. Material preparation

2.1.1. Preparation of the carbonaceous precursors with high ion-exchange capacity

All chemicals were of analytical grade and purchased from Sigma-Aldrich without any further purification. In a typical preparation process, a 70 mL aqueous solution of 0.6 M glucose was sealed into a 100 ml Teflon-lined stainless-steel autoclave and hydrothermally reacted at 190 °C for 24 h. The brown precipitate was washed and filtrated with deionized water and ethanol several times, and the obtained powders were dried at 80 °C overnight and identified as HC. Then, the brown solids (HC) were calcined in air in a range of temperatures from 200 °C to 350 °C for 5 h. The heat-treated solids were denoted as HC*x*, where *x* designated the heating temperature in °C. For comparison, a sample denoted as G300 was prepared directly via the calcination of glucose at 300 °C.

2.1.2. Preparation of ultramicroporous carbon nanospheres

Typically, the carbonaceous precursors (HC, HC*x*, and G300) were added into the aqueous KOH solution with a 1:1 mass ratio of KOH to precursors. After stirring at 80 °C for 6 h, the mixture was filtered and the solid materials were separated and thoroughly washed with deionized water until a neutral pH was achieved. The ion-exchanged samples were dried in a vacuum oven at 80 °C for 8 h and denoted as IE-HC*x*. Then the powder was carbonized at 800 °C for 1.5 h with a heating rate of 3 °C min^{-1} in argon. Finally, the resulting samples were immersed in excess amounts of dilute HCl solution under stirring, and then washed with deionized water until neutral pH. The resulting chemically activated porous carbons were denoted as CA-G300, CA-HC and CA-HC*x*.

2.2. Material characterization

Microscopic morphology, energy dispersive spectroscopy (EDS) of carbons were collected by a scanning electron microscope (SEM; FEI Quanta FEG 250 ESEM) and transmission electron microscope (TEM/STEM; JEOL, JEM-2010F, 200 kV) equipped with a large solid angle for high X-ray throughput, scanning, scanning-transmission and a Gatan imaging filter for energy filtered imaging. The chemical compositions were determined by using an elemental analyzer (EA, ElementarVario EI III, Elementar), Fourier transform infrared spectroscopy (FT-IR, Nicolet 6700) and X-ray photoelectron spectroscopy (XPS, PHI 5000 VersaProbe, ULVAC-PHI). Raman spectra were collected by a LabRAM HR800 from JY Horiba. X-ray diffraction (XRD) was performed on the X-ray diffractometer (MiniFlex 600, Rigaku). The potassium content was tested by the inductively coupled plasma - optical emission spectrometer (ICP-OES). Thermogravimetric analysis (TGA) was carried out on a thermogravimetric analyzer (NETZSCH STA 409 thermobalance) with a heating rate of 5 °C min^{-1} in air. The content of carboxyl group on carbons was examined by Boehm titrations [26]. N_2 adsorption-desorption isotherms were measured at liquid nitrogen temperature (−196 °C) and CO_2 adsorption was performed at 0 °C by using a surface area and porosity analyzer (ASAP 2020M, Micromeritics). Prior to sorption measurements, the carbon samples were degassed at 300 °C for 4 h. The BET equation was used to calculate the total specific surface area from N_2 adsorption data obtained in the relative pressure range of 0.05–0.25. Total pore volume was obtained at a relative pressure of 0.998. Micropore surface area and micropore volume were calculated by the t-plot method. CO_2 adsorption data obtained at 0 °C was employed to calculate ultramicropore volume and mean pore size. For advanced porosity analysis, pore size distributions were determined via the quenched solid state density functional theory (QSDFT) method, with sorption of nitrogen at −196 °C and slit-like pores acting as the model adsorbent and pore model, as well as the non-local density functional theory (NLDFT) method with CO_2 at 0 °C and slit-like pores as the pore model. It should be noted that microscopic methods based on statistical mechanics, such as NLDFT and QSDFT, allow describing the configuration of the adsorbed phase on a molecular

level and are currently acknowledged as the most accurate methods [27–30].

2.3. CO_2 capture measurements

The CO_2 adsorption measurements were performed on a Micromeritics ASAP 2010 static volumetric analyzer at 0 °C and 25 °C. Prior to the measurement, the carbon samples were degassed at 300 °C in vacuum for 4 h. The adsorption capacity was investigated by exposing the quantitative amount of CO_2 with a concentration of 99.99% and calculated in terms of adsorbed amount per gram of sample in the pressure range of 0.001 bar−1 bar.

2.4. Model and computational methods

Grand canonical Monte Carlo (GCMC) simulations were carried for the adsorption of CO_2 at 25 °C and 1 bar in graphite slit pores. In this work, the porous carbon-based material was represented by a three-layer graphite slab [31]. CO_2 was represented as a three-site rigid molecule by the TraPPE model [32], and its intrinsic quadrupole moment was described by a partial-charge model. The C=O bond length was 1.16 A, and the bond angle O=C=O was 180°. The intermolecular interactions of CO_2 and CO_2 were modeled by Lennard-Jones (LJ) potentials. The standard Lorentz-Berthelot mixing rules were used to calculate the cross LJ interaction parameters and the potential energies. The framework of graphite was treated as rigid since the geometries of the framework were not significantly influenced by CO_2 adsorption. The potential parameters for force field calculations are shown in Table 1.

In the GCMC simulations, the number of trial moves was 4×104, in which the first 15000 moves were used for equilibration and the second 25000 moves for production. The LJ interactions were evaluated using a spherical cutoff of 12 Å with the long-range corrections added. Five types of trail moves were attempted for CO_2 molecules: randomly attempted, rotation, partial regrowth (neighbouring positions), complete regrowth (new positions) and a swap between reservoirs (including creation and deletion). The GCMC simulations were performed in RASPA package [33].

3. Results and discussion

3.1. Formation of ultramicroporous carbon nanospheres

Fig. 1 illustrates the synthetic route of the ultramicroporous carbon nanospheres. The initial stage of the preparation is marked by the hydrothermal carbonization of aqueous glucose solution, during which oxygen-containing functional groups, including a small quantity of carboxyl groups, are created on the surface of carbon nanospheres as the initial active sites for further oxidation. Following this, a simple heat treatment at a low temperature in air is performed to transform the active sites located on the surface of the hydrochars into carboxyl group, which acts as the abundant active binding sites for ion exchange. At this stage, the number of carboxyl groups increases significantly to deliver a high ion-exchange capacity. Subsequently, an ion exchange reaction is conducted between carbon nanospheres rich in carboxylic acid groups and KOH solution, after which plentiful and uniformly dispersed carboxylates (−COOK) are generated on the outer layer of carbon particles. After ionic activation, the uniform ultramicropores are produced. The in-situ intercalation of potassium ions in a homogeneous distribution promotes efficient and uniform activation effect. This synthesis route does not demand the input of additional activating agents and chemicals.

Table 1
Potential parameters for force field calculations.

Species	Lennard-Jones potentials				Bond length	Bending angle
	Site	σ (Å)	ε/k_B (K)	q (e)		
CO_2	C	2.80	27.0	0.70	$r_{C-O} = 1.16$ Å	$\theta_{\angle OCO} = 180°$
	O	3.05	79.0	−0.35		
C (graphite)	C	3.40	28.0	0		

3.2. Structural and chemical properties of carbonaceous materials with high ion-exchange capacity

The microscopic morphology and structure of the carbonaceous precursors were imaged by SEM and TEM. To show the advantage of the combined hydrothermal and oxidative treatment method, glucose is directly calcined at 300 °C (G300) for comparison. In Fig. 2a, G300 exhibits a plate-like structure with smooth carbon sheets stacked together, as indicated by SEM images in Fig. S1a. Fig. 2b shows a representative TEM image of hydrochars (HC) obtained via hydrothermal treatment of glucose that possesses regular carbon nanospheres with a uniform diameter of 400 nm. As shown in Fig. S1b, HC exhibits compact spherical morphology with a uniform dispersion, and no apparent cracks and pores are found in the smooth surface. The completely different morphology between G300 and HC indicates that the hydrothermal treatment promotes the formation of carbonaceous particles with regular spherical morphologies. As shown in Fig. 2c and Fig. S1c, there are not apparent changes in the morphology after HC experiences calcination treatment in air at 300 °C, and the spherical geometry is still retained. The adhesion between particles slightly increases, leading to an improved particle-particle contact, due to the formation of surface oxygen-containing functional groups in the heat treatment.

EA is conducted to investigate the chemical composition of the carbonaceous materials, as summarized in Table S1. Both of G300 and HC show a low oxygen content, with the low O/C atomic ratio of 0.37 and 0.33, respectively. The samples experiencing the combined hydrothermal and oxidative heat treatment (HC*x*) display a significant increase in oxygen content while a steady reduction in hydrogen content with increasing heat-treatment temperature. Therefore, more oxygen-containing functional groups are formed during the oxidative heat treatment, and the amount of oxygen-containing functional groups increases as the heating temperature rises. To further investigate the chemical characteristics of the carbonaceous materials, FT-IR analysis is performed (Fig. 2d). All samples are rich in oxygen-containing functional groups such as carbonyl, hydroxyls, carboxyl, and esters. The characteristic absorption bands for all the samples correspond to −OH bending and C−OH stretching vibrations at 1040 cm^{-1}, carboxyl anhydride groups stretching vibrations near 1260 cm^{-1}, and C=C stretching vibrations in aromatic groups at 1600 cm^{-1}. A broad absorption band located between 3000 and 3700 cm^{-1}, which is attributed to O−H stretching vibrations of hydroxyl or carboxyl groups, also demonstrates the presence of residual hydroxyl groups which make up the hydrophilic surface [34]. Of particular note is the increased intensity of the adsorption bands around 1710 cm^{-1} corresponds to C=O vibration in carboxyl group, which comes from the hydrothermal carbonization of glucose and oxidizing functionalization [35–37]. These results provide direct evidence that more carboxyl groups are generated onto the surface of carbonaceous precursor in the combined method of hydrothermal and oxidative heat treatment. The significant increase in the content of carboxyl group from HC to HC*x* demonstrates that more active sites located on hydrochars are transformed into carboxyl groups via calcination in air. Especially the transformation is remarkably

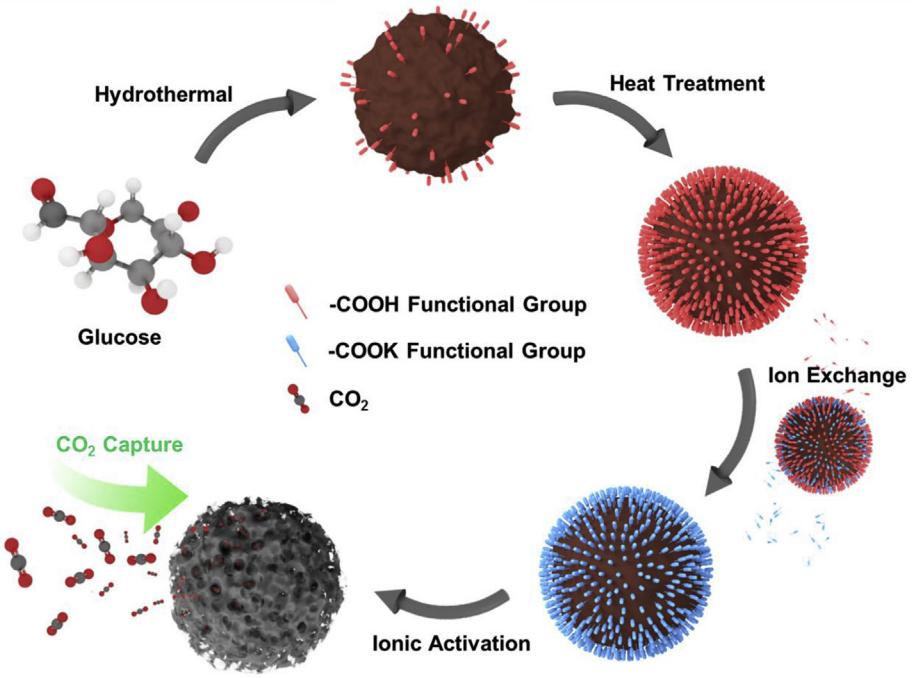

Fig. 1. Schematic diagram of the synthesis of ultramicroporous carbon nanospheres. (A colour version of this figure can be viewed online.)

enhanced with the increase in heat-treatment temperature, resulting in plentiful −COOH groups present in HC300.

XPS analysis is also performed to further determine the chemical composition of carbonaceous precursors. As displayed in Fig. 2e, four individual fitted signals in the C 1s spectrum are observed in each sample: aromatic/aliphatic carbon groups (C−C/C=C, CH_x, 284.8 eV, Peak I), hydroxyl groups (−C-OR, 285.9 eV, Peak II), carbonyl groups (>C=O, 287.0 eV, Peak III), and carboxylic groups, lactones, or esters (−COOR, 288.9 eV, Peak IV) [38–40]. These results confirm abundant oxygen groups present in the shells of the carbonaceous materials. In comparison with the corresponding peaks of HC, the Peak IV intensity of HC300 is noticeably increased. Peak-fitting data for the C 1s peak areas of as-prepared samples is summarized in Table S2. The percentage of Peak IV attributed to −COOR in HC300 is much larger than that of HC (10.53% vs. 4.80%). These results show that more oxygen-containing functional groups and, more importantly, a larger number of carboxylic acid groups form on the outer layer during the heat-treatment process. Although there are carboxyl groups found on G300 after direct calcination at 300 °C, its amount is far lower than that of HC300. From this result, it can be inferred that the large increase of carboxyl group on HC300 is not due to incomplete carbonization of glucose. These findings from XPS analysis and FT-IR spectra are also in good agreement with the EA results. The content of carboxyl groups on carbonaceous precursors are further examined by Boehm titrations [26], indicative for ion-exchange capacity. As shown in Fig. 2f, the ion-exchange capacity increases with increasing calcination temperature. HC300 exhibits an extremely high ion-exchange capacity (3.92 mmol g^{-1}), almost 18 and 6 times higher than G300 and HC, respectively. This result provides direct quantitative evidence for abundant carboxyl groups on carbonaceous materials, which also validates the crucial role of oxidative heat treatment in improving the amount of carboxyl group.

The porosity of carbonaceous precursors was investigated by N_2 adsorption/desorption. In Fig. S2, HC showed a very low surface area of only 9.6 $m^2 g^{-1}$ and pore volume of 0.018 $cm^3 g^{-1}$. After heat treatment, HC300 also exhibited the poor porosity with a low surface area of 6.7 $m^2 g^{-1}$ and pore volume of 0.017 $cm^3 g^{-1}$. Therefore, the carbonaceous materials before the ion exchange possess the extremely low porosity, which further indicates the great capability of the ionic activation methodology in constructing highly porous structure.

This facile synthesis strategy not only paves a new way to employ carbon with abundant carboxyl group, but also makes it feasible to tune the content and the size of ultramicropores by controlling the heating temperature, hence providing great potential to design porous carbonaceous materials toward optimal performance. During the oxidative heat treatment, the enriched carboxyl group comes from the oxidation of glucose dehydration products, which are obtained from the hydrothermal process. The C=C band of non-aromatic groups in hydrochar lost electrons to form free radicals when heated, which then react with oxygen to generate positive ion radicals containing two oxygen atoms. Next, a free radical chain reaction is triggered between the positive ion radicals and non-aromatic groups with C=C band, meanwhile producing new free radicals to repeat this process. Subsequently, the four-membered ring units with two oxygen atoms are created through the cyclization reaction of free radical products, and rapidly decompose into aldehyde or ketone [35,41]. Ultimately, abundant carboxyl groups are formed via oxidation of aldehyde with the participation of water and oxygen in the air during the heat-treatment procedure. Moreover, the increased heat treatment temperature triggers a violent free radical reaction, producing a larger amount of aldehyde or ketone, which facilitates the carboxyl enrichment on the carbon.

Even though the content of carboxyl groups is increased with the rising heat-treatment temperature, the yield productivity and weight loss of heated carbonaceous materials also need to be considered. The weight loss ratios of HC after heat treatment at varying temperatures are summarized in Fig. S1d. The weight loss ratio reaches almost two-thirds of the original HC weight when the

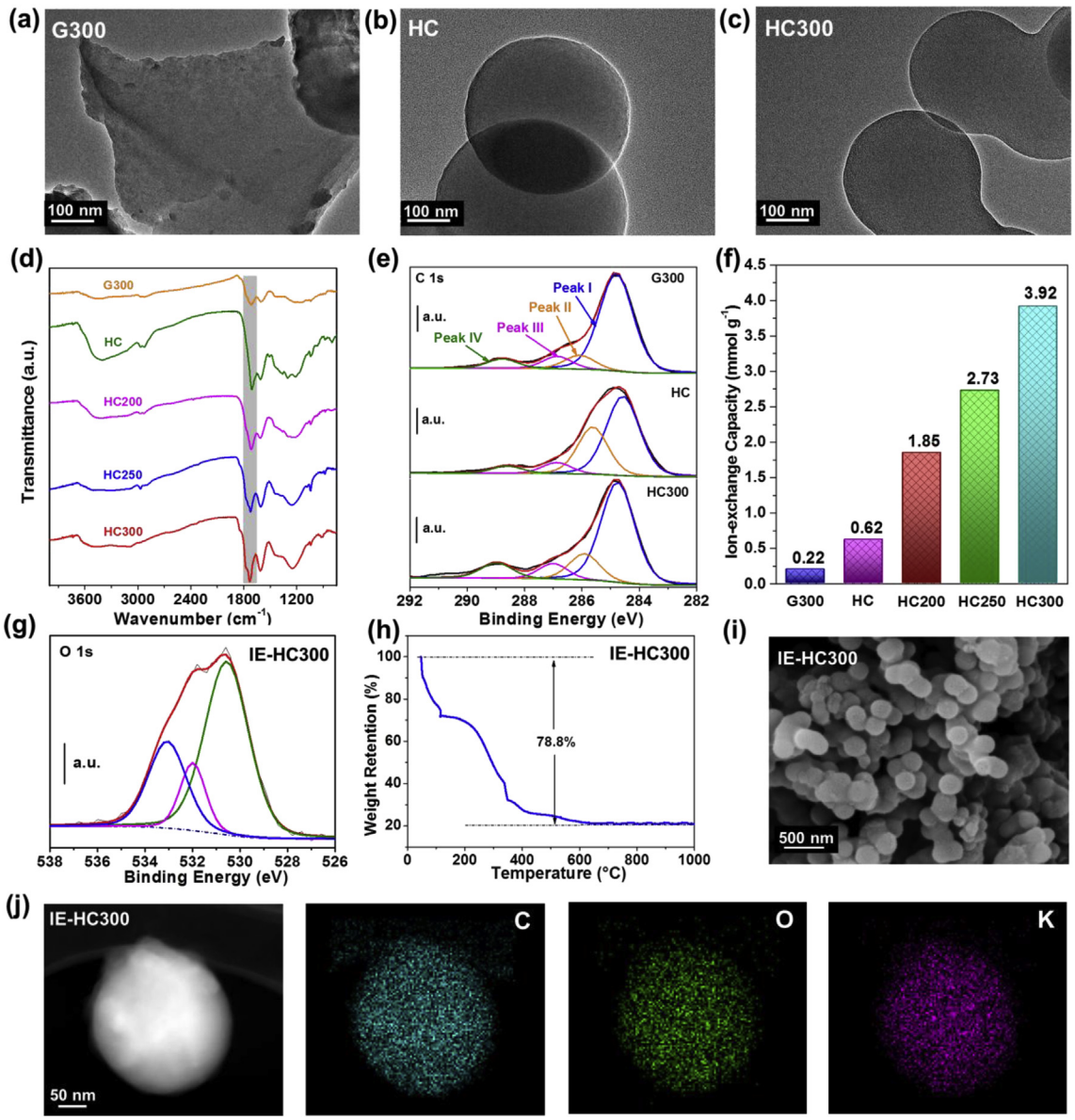

Fig. 2. TEM images of: (a) G300, (b) HC and (c) HC300. (d) FT-IR spectra for carbonaceous precursors (the grey-shaded region highlights the −COOH peak). (e) XPS C1s spectra of G300, HC and HC300. (f) Ion-exchange capacity in carbonaceous precursors determined by Boehm titrations. (g) XPS O1s spectrum of IE-HC300. (h) TGA in air of IE-HC300. (i) SEM images of IE-HC300. (j) STEM and elemental mapping images of IE-HC300. (A colour version of this figure can be viewed online.)

temperature increases to 350 °C though the carboxyl group content increases slightly to 4.02 mmol g^{-1}, while the weight loss ratio is only 37.4% when heated at 300 °C. Higher weight loss occurs with the increase of calcination temperature, presumably because several incompletely polymerized monomers/oligomers or small molecules on the HC frameworks experienced decomposition and volatilization [35]. Considering the above mentioned two factors, as well as physical/chemical stability, the heat-treatment temperature of 300 °C is the optimal for the oxidizing functionalization of HC.

3.3. Physical and chemical properties of ultramicroporous carbon nanospheres by ionic activation

During the ion exchange process, −COOK acting as the ionic activation agent is formed by the reaction of K^+ ions and carboxylic acid groups, which leads to the in-situ immobilized K^+ ions onto the surface of the carbonaceous materials in a homogenous distribution. Compared to the conventional chemical activation via simply physical mixing with activating agents, herein the uniform dispersion of K^+ ions contributes to a homogeneous and efficient ionic activation in the pyrolytic etching process. Besides, a very few K^+ ions may be incorporated with carbonaceous materials due to the weak electrostatic effect. However, the ion exchange effect is dominant compared to the weak electrostatic interaction.

XPS O 1s analysis of ion-exchanged HC300 (IE-HC300) is performed. Three main peaks can be identified in Fig. 2g. The peaks appearing at 531.8 eV and 532.8 eV are assigned to carbonyl groups and carboxyl groups, respectively [42]. An apparent strong peak around 530.5 eV is assigned to the K—O bond. The content of potassium intercalated into IE-HC300 is 16.0 wt% corresponding to 4.10 mmol g^{-1} (Table S1) as determined by ICP-OES and TGA in air (Fig. 2h), which is very close to the content of carboxyl in HC300 (3.92 mmol g^{-1}). This also confirms the high efficiency of ion

exchange process and some level of electrostatic effect. After ion exchange, the hydrogen content in IE-HC300 reduces considerably compared to HC300, demonstrating that H^+ in carboxyl group is exchanged with K^+. The ion exchange process does not change the morphology of carbonaceous materials, as revealed by a representative SEM image (Fig. 2i) and high-angle annular dark field (HAADF) STEM image (Fig. 2j) of IE-HC300, which still retains spherical morphology with smooth surface and uniform size. The corresponding EDS mapping (Fig. 2j and Fig. S1e) confirms the presence of elements C, O and K. The homogeneous distribution of K indicates that the successful intercalation of K^+ ions via ion exchange, while the uniform dispersion of O confirms presence of plentiful oxygen-containing functional groups. These qualitative and quantitative analysis (high exchanged K content: 16.0 wt%) corroborates the high ion-exchange capacity of HC300.

In ionic activation, −COOK experiences initial thermal decomposition in the temperature range of 200–400 °C with the formation of K_2CO_3. From 400 °C to 600 °C, potassium carbonate is continuously transformed into K_2O which severely etches the carbon framework into CO and K to generate ultramicroporosity above 800 °C. Meanwhile, potassium vapor may permeate between carbon layers, causing swelling and disintegration of the carbon micro-structure, which consequently produces even more ultramicroporosity, as shown in Fig. S3a [13]. The structural evolution and pore texture of the final activated ultramicroporous carbons after high-temperature activation are displayed in Fig. 3. CA-G300 exhibits a highly aggregated and wrinkled laminar structure stacked by two-dimensional carbon sheets (Fig. 3a,d). However, CA-HC and CA-HC300 still maintain the regular spherical morphology (Fig. 3b,c,e,f). The ionic activation process exhibits the advantage of well maintaining the structure integrity. For CA-HC300, the slight agglomeration and adhesion between carbon nanospheres remains present (Fig. 3c,f). The enhanced oxidative functionalization and oxygen-containing functional groups on the surface derived from the heat-treatment process can boost the interaction force between particles and tend to bind carbon nanospheres together, facilitating secondary self-assembly processes during the ionic activation which is beneficial for the formation of interconnected pore structures. When observed by TEM (Fig. 3g,h,i), the as-synthesized carbons possess highly connected and plentiful worm-like micropores without obvious mesopore or macropore signs. These uniform micropores result from the activation of highly dispersed potassium ions.

XPS is performed to investigate the chemical characteristics of ultramicroporous carbon. In Fig. 4a, four individual peaks are observable in the C 1s signal, containing aliphatic/aromatic carbon groups (C–C/C=C, CH_x, 284.8 eV), hydroxyl groups (–C-OR, 285.9 eV), carbonyl groups (>C=O, 287.0 eV), and carboxylic groups, lactones, or esters (–COOR, 288.9 eV). Clearly, in comparison with the corresponding peak of HC300 in Fig. 2e, the intensity of the peak attributed to carboxylic groups in CA-HC300 decreases significantly. The integrated peak areas are listed in Table S2, indicating that the amount of carboxylic group declines noticeably compared to that of HC300. This is because carboxylic groups present in the form of –COOK decompose into potassium carbonate in the initial process of ionic activation, and then most of the potassium carbonate experience thermal decomposition to form potassium oxide that ultimately produces microporosity by etching carbon atoms on the framework. Two strong peaks present in the O 1s spectrum at 531.8 eV and 532.8 eV are observed in Fig. 4b, belonging to carbonyl groups and carboxylic groups, respectively. It should be noted that the strong peak appearing at 530.5 eV in Fig. 2g, attributable to the K–O bond in IE-HC300, is no longer found here because the potassium ions are washed away. The Raman spectra for the carbons are exhibited in Fig. 4c. The peak at 1580 cm^{-1} (G-band), assigned to the E_{2g} mode of graphite and related to the vibration of C sp^2-bonded atoms, indicates the ideal graphitic lattice of carbons. The peak at 1355 cm^{-1} (D-band) corresponds to vibrations of C atoms with dangling bonds in planar terminations of disordered graphite [43]. The carbon framework for all the obtained carbons is clearly highly graphitized (Fig. 4c), with an I_D/I_G of 0.9. The crystalline structures of ultramicroporous carbons were investigated by XRD (Fig. S4). Two broad diffraction bands centered at 23.4° and 43° correspond to the reflections of the

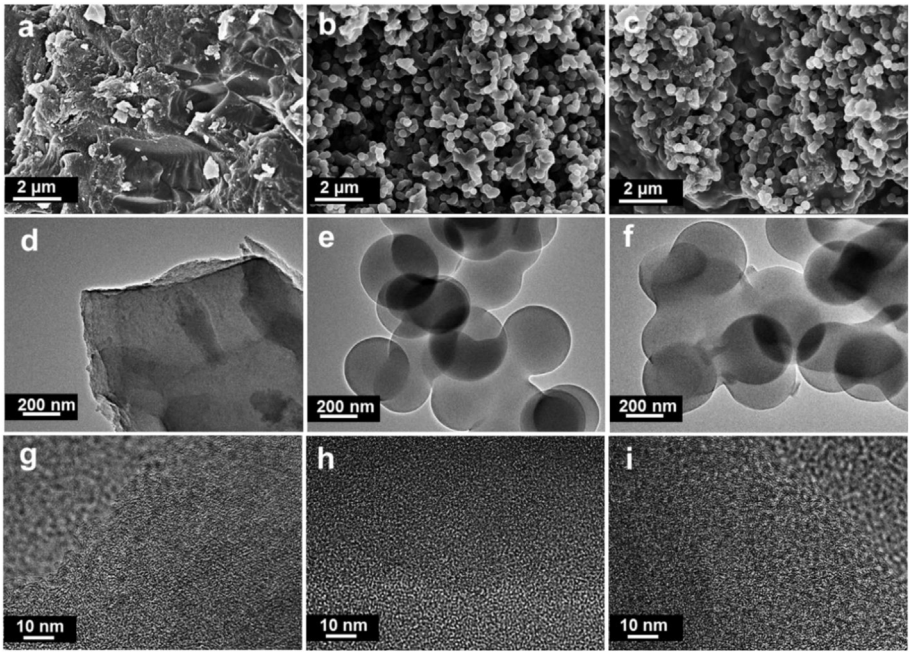

Fig. 3. SEM images of: (a) CA-G300, (b) CA-HC and (c) CA-HC300. TEM images of: (d, g) CA-G300, (e, h) CA-HC and (f, i) CA-HC300.

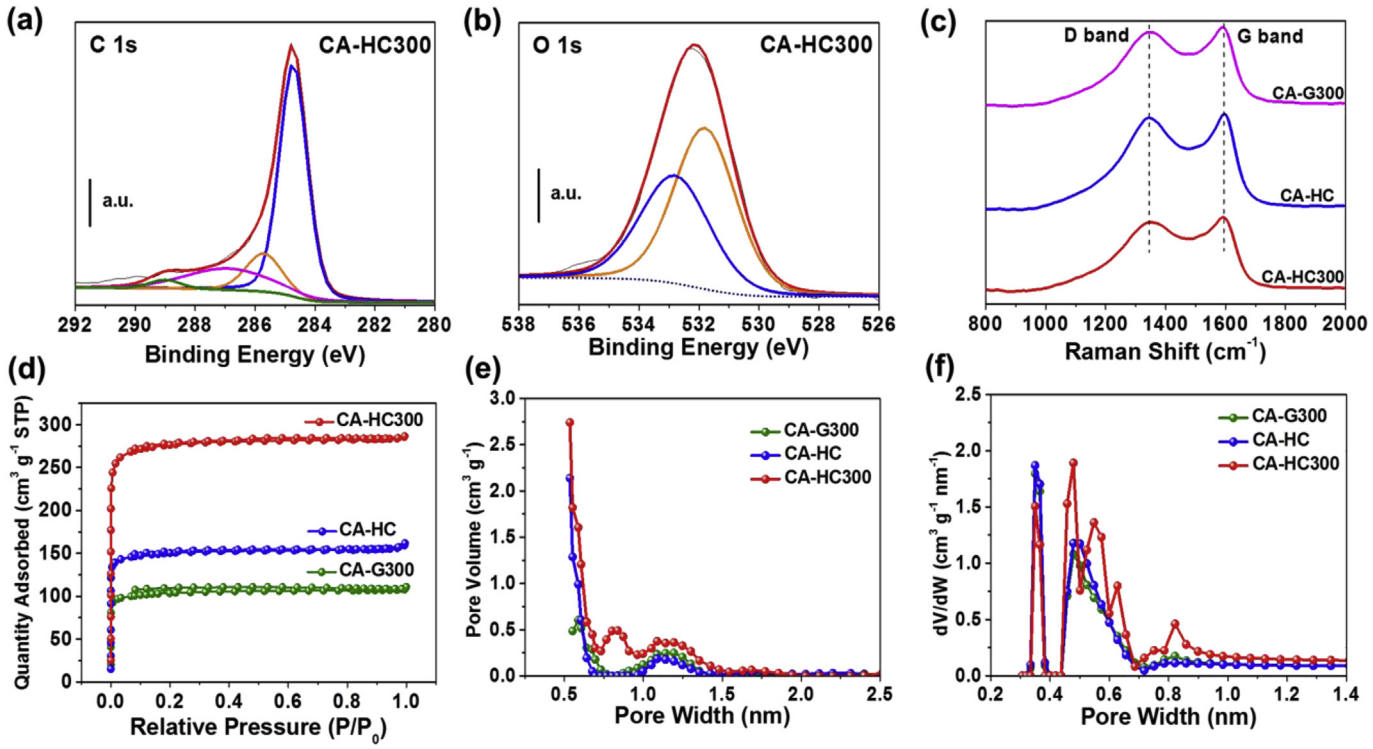

Fig. 4. (a) XPS C 1s spectrum of CA-HC300. (b) XPS O 1s spectrum of CA-HC300. (c) Raman spectra of CA-G300, CA-HC and CA-HC300. (d) N_2 adsorption-desorption isotherms at −196 °C. (e) QSDFT pore size distributions derived from N_2 sorption. (f) NLDFT pore size distributions derived from CO_2 sorption. (A colour version of this figure can be viewed online.)

(002) and (101) graphitic planes, which is typical for activated carbon materials.

The porosity properties of the prepared ultramicroporous carbons were investigated by N_2 and CO_2 adsorption/desorption analysis at −196 °C and 0 °C, respectively. As shown in Fig. 4d and Figs. S3b and a typical type-I N_2 adsorption isotherm is observed for all the prepared carbons with a narrow knee at very low relative pressure ($P/P_0 < 0.02$). No obvious adsorption increment is found at higher relative pressure when achieving a high adsorption plateau, indicating micropores are dominant in these carbons after ionic activation. This is also confirmed by the narrow pore size distribution derived from N_2 adsorption using QSDFT method (Fig. 4e and Fig. S5a). It should be noted that CA-HC300 possesses more abundant ultramicropores (~0.5 nm) than the other carbons, as displayed in Fig. 4f and Fig. S5b, measured via NLDFT method using CO_2 as the probe gas.

As summarized in Table 2, the porosity of CA-G300 is quite undeveloped with a relatively low surface area of 324 $m^2 g^{-1}$ and pore volume of 0.24 $cm^3 g^{-1}$. The carbons that experienced hydrothermal carbonization (CA-HC and CA-HC*x*) possess more developed pore structure than CA-G300. The specific surface area and pore volume of CA-HC300 almost double compared to CA-HC, achieving 862 $m^2 g^{-1}$ and 0.44 $cm^3 g^{-1}$, respectively. While CA-HC and CA-HC*x* exhibit relatively moderate specific surface areas (470–923 $m^2 g^{-1}$), these carbons possess a considerable proportion of ultramicropores in the range of 72.0%–95.5%, demonstrating the ultramicroporous nature in the prepared carbons for this work. Of particular note is that an extraordinarily high fraction (95.5%) of ultramicropores is observed in CA-HC300, which presents a mean pore size of 0.5 nm. Although CA-HC350 shows higher total pore volume and specific surface areas than CA-HC300, CA-HC300 exhibits significantly higher ultramicropore volume. Besides, the

Table 2
Textural properties of the series of prepared carbons.

Samples	N_2 sorption at −196 °C				CO_2 sorption at 0 °C		
	S_{BET}[a] ($m^2 g^{-1}$)	S_{micro}[b] ($m^2 g^{-1}$)	V_T[c] ($cm^3 g^{-1}$)	V_{micro}[b] ($cm^3 g^{-1}$)	V_{ultra}[d] ($cm^3 g^{-1}$)	F_{ultra}[e] (%)	$M_{pore\ size}$[d] (nm)
CA-G300	324	276	0.24	0.14	0.18	75.0	0.43
CA-HC	470	409	0.25	0.22	0.20	84.0	0.43
CA-HC200	518	449	0.27	0.23	0.23	85.2	0.44
CA-HC250	622	560	0.32	0.29	0.28	87.5	0.47
CA-HC300	862	763	0.44	0.42	0.42	95.5	0.50
CA-HC350	923	830	0.50	0.46	0.36	72.0	0.80

[a] Brunauer-Emmett-Teller surface area (S_{BET}) was calculated using the N_2 adsorption isotherm data within the relative pressure from 0.05 to 0.25.
[b] Micropore surface area (S_{micro}) and micropore volume (V_{micro}) were calculated by the t-plot method.
[c] Total pore volume (V_T) was obtained at $P/P_0 = 0.998$.
[d] Cumulative volume of ultramicropores <0.7 nm (V_{ultra}) and mean pore size ($M_{pore\ size}$) were determined by CO_2 sorption (0 °C) using NLDFT method with a slit-shaped pore model.
[e] Fraction of ultramicropores (F_{ultra}) was determined by the proportion of ultramicropore volume in the total pore volume.

specific surface area, micropore volume and total pore volume of CA-HC*x* steadily increase when heated with increasing temperatures, especially the ultramicropore volume reaches the highest value (0.42 $cm^3 g^{-1}$) in CA-HC300. This is indicative for the positive effect of the enhanced carboxyl group on well-developed ultramicroporous structure formed in ionic activation. This is because that the oxidative heat treatment in air forms more abundant carboxyl groups and meanwhile delivers a high ion-exchange capacity, which increases the ion-exchange efficiency of potassium ions, thus promoting the formation of advanced and uniform ultramicropores during the ionic activation process. Moreover, it is worthy to note that ultramicropore volume of CA-HC350 decreases to 0.36 $cm^3 g^{-1}$ compared to CA-HC300 (0.42 $cm^3 g^{-1}$), which leads to a significant reduction on ultramicropore fractions from 95.5% to 72.0%. This indicates wider micropores (>0.7 nm) are formed in CA-HC350, and this slight pore enlargement is presumably due to the over-activation with excess exchanged potassium ions for CA-HC350. Therefore, an optimum ion-exchange capacity can not only produce developed ultramicropore structure, but tune the ultramicropore content and pore size.

3.4. CO_2 capture performance and CO_2 adsorption mechanism in ultramicropores

The CO_2 adsorption measurements of the synthesized ultramicroporous carbon nanospheres are performed at 0 and 25 °C (Fig. 5a and b and Fig. S6). As recorded in Table 3, CA-HC300 exhibits the nontrivial capacities of 5.91 and 4.30 mmol g^{-1} at 0 °C and 25 °C under atmospheric pressure, respectively. In particular, the designed carbons show an extremely high CO_2 capacity of 1.58 mmol g^{-1} at the typical flue gas condition (25 °C and CO_2 partial pressure of 0.15 bar). To the best of our knowledge, these uptake values are much higher than those recorded for most of the reported carbon materials for CO_2 capture under identical conditions (Table S3), even including known N-doped porous carbons that are regarded as excellent CO_2 adsorbents [44–47]. Furthermore, based on a recent review regarding CO_2 capture on metal-organic frameworks (MOFs) [48], these values are higher than many MOFs, including YO-MOF [49], bio-MOF-11 [50], and Zn/DOBDC [51].

Table 3
CO_2 sorption capacities of carbons at different temperature and pressure.

Sample	CO_2 sorption capacity (mmol g^{-1})		
	0 °C P = 1 bar	25 °C P = 1 bar	25 °C P = 0.15 bar
CA-G300	4.46	3.16	1.31
CA-HC	4.69	3.31	1.36
CA-HC200	4.51	3.31	1.58
CA-HC250	4.60	3.37	1.43
CA-HC300	5.91	4.30	1.44
CA-HC350	5.43	3.54	1.16

It is of great interest that CA-HC300 exhibits an extremely high CO_2 capacity, while only exhibiting a moderate surface area and porosity ($S_{BET} = 862\ m^2 g^{-1}$, $V_T = 0.44\ cm^3 g^{-1}$) compared to CA-HC350 ($S_{BET} = 923\ m^2 g^{-1}$, $V_T = 0.50\ cm^3 g^{-1}$) and many reported porous carbons (Table S3). This is because CA-HC300 possesses an extraordinarily high content of ultramicropores (95.5%), which plays a key role in efficient CO_2 capture.

To better understand the adsorption mechanism and reveal the superiority of ultramicropores on enhancing CO_2 molecules adsorption within the pore structure, movies of CO_2 uptakes in the perfect graphite slit pores of different pore widths are studied by theoretical calculation based on the GCMC simulation. Comparing adsorbed-CO_2 density in three kinds of graphitic pore structure models (Fig. 5d,e,f and Fig. S7), the best pore width of three kinds of microporous carbons for CO_2 capture is 0.5 nm. The trend of the simulation results agrees fairly well with the experimental data, that CA-HC300 possessing an ultrahigh content of ultramicropores

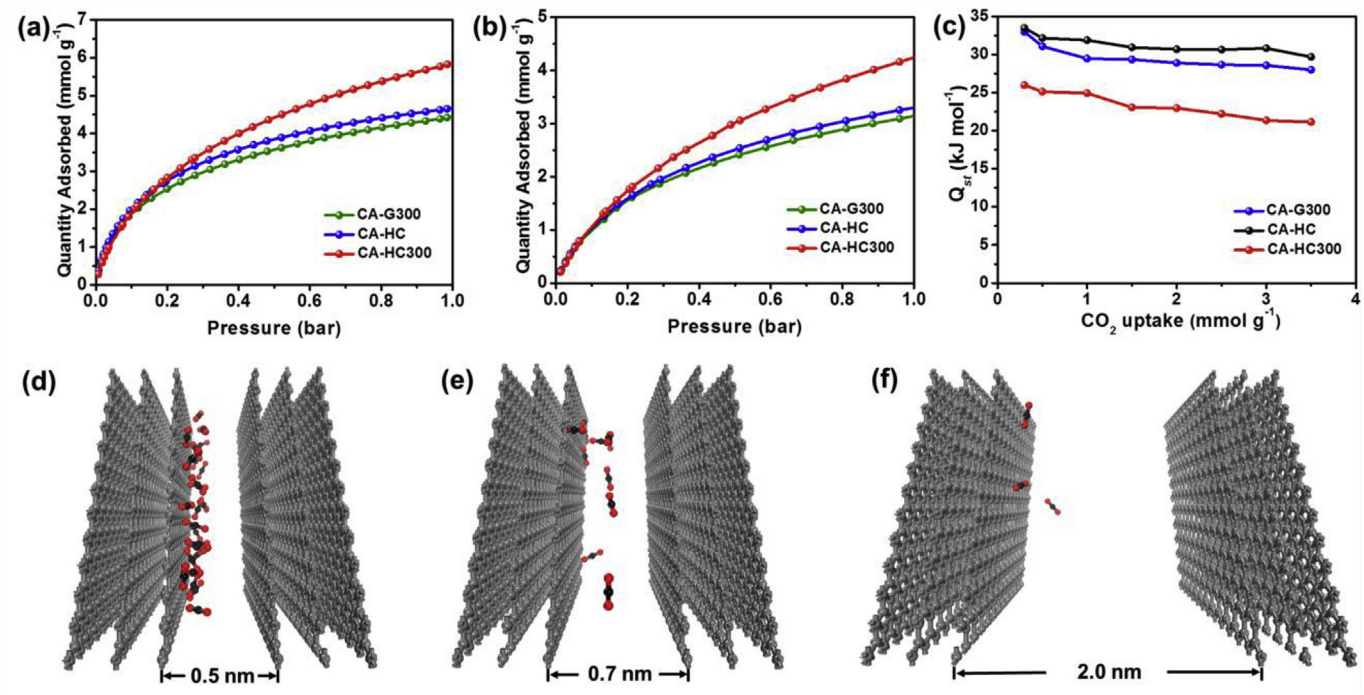

Fig. 5. CO_2 sorption isotherms at: (a) 0 °C and (b) 25 °C. (c) Isosteric heats of CO_2 sorption isotherms. Comparisons for movies of CO_2 loading in the perfect graphite slit pores with pore width of: (d) 0.5 nm, (e) 0.7 nm and (f) 2.0 nm derived from molecular simulations based on GCMC. (A colour version of this figure can be viewed online.)

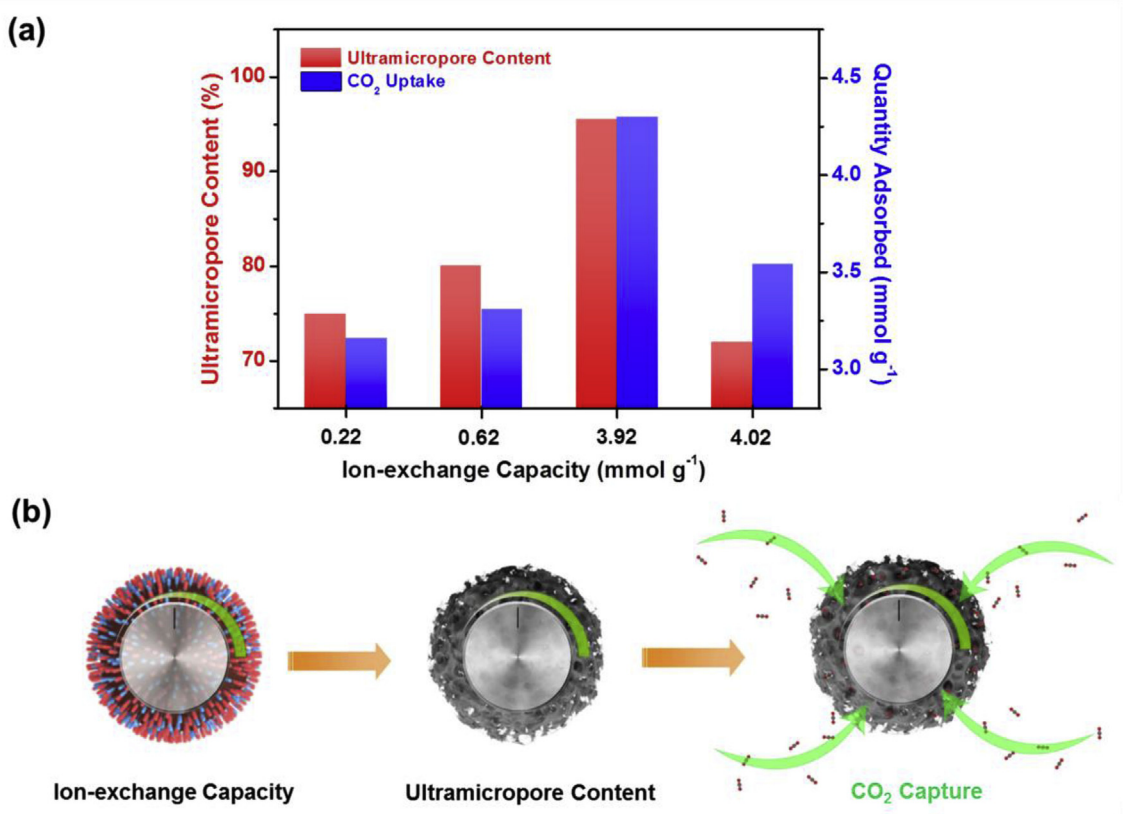

Fig. 6. (a) Relationship between ion-exchange capacity, ultramicropore content and CO_2 uptake. (b) Schematic diagram of controllable design from surface functionality to pore structure tunability and finally toward performance. (A colour version of this figure can be viewed online.)

with a mean pore size of 0.5 nm exhibit the highest CO_2 capacity. It is important to note that the loading amount of CO_2 adsorption would decrease with the width of silt pores increasing, because of the decreasing overlapping potentials of the wall-wall interactions and CO_2-wall interaction in the graphite pores. The CO_2 adsorption uptake at low pressures mainly depends on the volume of narrow ultramicropores instead of the specific surface area and total pore volume. The adsorbent-adsorbate interaction energy, derived from short-range attractive and repulsive forces, is significantly reinforced when the adsorption occurs in extraordinarily fine pores due to the overlapping of potential fields from neighbouring walls [52]. The enhanced adsorption potential, therefore, results in the complete filling of fine micropores at low relative pressure (<0.01). The adsorption mechanism consists of volume-filling rather than surface cover typical of meso/macroporous materials and the adsorbates occupying these fine micropores are in a liquid-like state [53]. For this reason, the interaction between adsorbents and CO_2 becomes stronger when the pore size decreases. Therefore, these plentiful and homogeneous ultramicropores of 0.5 nm act as the ideal places for CO_2 sorption to proceed.

When carrying out CO_2 sorption measurements at different temperatures, it was found that CO_2 uptake declines considerably with the increase of adsorption temperature as shown in Fig. 5a and b and Table 3. This is because CO_2 molecules have higher molecular kinetic energy at a higher temperature, which drives CO_2 to escape from the pore surface of adsorbents easily. It is well known that CO_2 is produced as a part of flue gas in numerous industrial processes (15% CO_2 at 1 bar of pressure). Thus, capturing CO_2 from flue gases at such low partial pressure is still a great challenge. The designed carbons in this work (CA-HC200, CA-HC300) show ultra-high CO_2 capture capacities up to 1.58 mmol g^{-1} at 0.15 bar, 25 °C, far outperforming other previously reported carbon materials (Table S3). Consequently, the as-designed carbons are highly promising candidates for capturing CO_2 from the flue gas, and they are prepared only using inexpensive biomass (*i.e.,* glucose) as the carbon precursor without the addition of any other chemicals or heteroatom doping, achieving the green synthesis. These enable this technology to deliver high viability for large-scale and sustainable fabrication.

In order to investigate the energy required for regeneration, as well as the interaction strength between CO_2 molecules and as-prepared carbon adsorbents, the isosteric heat of adsorption (Q_{st}) is calculated from the CO_2 adsorption data at 0 and 25 °C by using the Clausius-Claperon equation (Supplementary Information). As shown in Fig. 5c, the high Q_{st} values are observed at the initial adsorption stage (low CO_2 uptakes), ranging from 26.0 to 33.0 kJ mol^{-1}, which are higher than the previously reported values for typical carbon adsorbents [54–56]. This indicates that CO_2 molecules strongly interact with the pore surface as a result of the strong adsorption potential of the extremely narrow micropores. On the other hand, these Q_{st} values are much smaller than the energy needed for breaking covalent bonds, suggesting a low-energy and reversible desorption. In particular, CA-HC300 shows a relatively low Q_{st} (21.2–26.0 kJ mol^{-1}) which implies low energy consumption during regeneration. It can be inferred that the abundant and well-developed ultramicropores with a narrow pore size distribution (~0.5 nm) present in CA-HC300 give rise to the enhanced utilization of porosity of the carbon material. The tailored pore characteristics contribute to promising CO_2 capture performance at ambient temperature and pressure.

The controllable relationship in this design is unveiled quantitatively in Fig. 6a. The ultramicropore content is tuned via ion-

exchange capacity, and an optimal value for 95.5% is found in the 3.92 mmol g^{-1} ion-exchange capacity. Meanwhile, the CO_2 adsorption capacity trend is in line with ultramicropore content. Consequently, it is proved that adjusting ion-exchange capacity is an efficient and effective approach to tune up the adsorption behavior of carbon materials to maximize the CO_2 capture capacity. This strategy not only reveals the relationship of the ion-exchange capacity, ultramicroporosity and CO_2 adsorption capacity of ultramicroporous carbonaceous materials, but also achieves the controllable design from surface functionality to pore structure tunability and finally toward performance superiorities (Fig. 6b).

4. Conclusions

In summary, we developed a novel strategy based on the ionic activation to finely tune the ultramicroporosity for carbon materials. The ultramicroporosity tunability can be realized by the adjustable ion-exchange capacity in the oxidative treatment process. Abundant carboxyl groups are created in oxidative functionalization to deliver a high ion-exchange capacity (3.92 mmol g^{-1}), triggering the in-situ immobilization of potassium ions as activating agents on carbonaceous precursors, which promotes an efficient and uniform ionic activation process. The obtained carbon nanospheres were endowed with an ultrahigh content (95.5%) of ultramicropores and uniform pore distribution, which were employed as a high-efficiency adsorbent for CO_2 capture. They exhibit an extremely high CO_2 adsorption capacity up to 1.58 mmol g^{-1} at typical flue gas conditions and 4.30 mmol g^{-1} at 25 °C and ambient pressure, outperforming most of previously reported carbon sorbents. This work not only delivers an appealing and universal guideline to synthesize ultramicroporous carbon materials for CO_2 capture, but also unfolds a controllable design concept from surface functionality to pore structure tunability and ultimately toward performance superiorities, holding great potential in extensive fields such as water purification, catalysis, and energy storage.

Acknowledgements

This work was supported by the Natural Sciences and Engineering Research Council of Canada (NSERC), University of Waterloo, Waterloo Institute for Nanotechnology and the Canadian Centre for Electron Microscopy at McMaster University.

Appendix A. Supplementary data

Supplementary data to this article can be found online at https://doi.org/10.1016/j.carbon.2018.10.096.

References

[1] P.M. Cox, R.A. Betts, C.D. Jones, S.A. Spall, I.J. Totterdell, Acceleration of global warming due to carbon-cycle feedbacks in a coupled climate model, Nature 408 (2000) 184–187.
[2] R.S. Haszeldine, Carbon capture and storage: how green can black be? Science 325 (2009) 1647–1652.
[3] C.L. Quéré C, R.M. Andrew, P. Friedlingstein, S. Sitch, J. Pongratz, A.C. Manning, et al., Global carbon budget 2017, Earth Syst. Sci. Data 10 (2018) 405–448.
[4] D.M. D'Alessandro, B. Smit, J.R. Long, Carbon dioxide capture: prospects for new materials, Angew. Chem. Int. Ed. 49 (2010) 6058–6082.
[5] H.W. Kim, H.W. Yoon, S.-M. Yoon, B.M. Yoo, B.K. Ahn, Y.H. Cho, et al., Selective gas transport through few-layered graphene and graphene oxide membranes, Science 342 (2013) 91–95.
[6] S.J. Datta, C. Khumnoon, Z.H. Lee, W.K. Moon, S. Docao, T.H. Nguyen, et al., CO_2 capture from humid flue gases and humid atmosphere using a microporous coppersilicate, Science 350 (2015) 302–306.
[7] G.-P. Hao, W.-C. Li, D. Qian, G.-H. Wang, W.-P. Zhang, T. Zhang, et al., Structurally designed synthesis of mechanically stable poly (benzoxazine-co-resol)-based porous carbon monoliths and their application as high-performance CO_2 capture sorbents, J. Am. Chem. Soc. 133 (2011) 11378–11388.
[8] G.T. Rochelle, Amine scrubbing for CO_2 capture, Science 325 (2009) 1652–1654.
[9] F. Geyer, C. Schönecker, H.-J. Butt, D. Vollmer, Enhancing CO_2 capture using robust superomniphobic membranes, Adv. Mater. 29 (2017) 1603524.
[10] Z. Liu, Z. Zhang, Z. Jia, L. Zhao, T. Zhang, W. Xing, et al., New strategy to prepare ultramicroporous carbon by ionic activation for superior CO_2 capture, Chem. Eng. J. 337 (2018) 290–299.
[11] Y. Li, B. Zou, C. Hu, M. Cao, Nitrogen-doped porous carbon nanofiber webs for efficient CO_2 capture and conversion, Carbon 99 (2016) 79–89.
[12] G.-P. Hao, Z.-Y. Jin, Q. Sun, X.-Q. Zhang, J.-T. Zhang, A.-H. Lu, Porous carbon nanosheets with precisely tunable thickness and selective CO_2 adsorption properties, Energy Environ. Sci. 6 (2013) 3740–3747.
[13] J. Zhou, Z. Li, W. Xing, H. Shen, X. Bi, T. Zhu, et al., A new approach to tuning carbon ultramicropore size at sub-angstrom level for maximizing specific capacitance and CO_2 uptake, Adv. Funct. Mater. 26 (2016) 7955–7964.
[14] V. Presser, J. McDonough, S.-H. Yeon, Y. Gogotsi, Effect of pore size on carbon dioxide sorption by carbide derived carbon, Energy Environ. Sci. 4 (2011) 3059–3066.
[15] Z. Zhang, J. Zhou, W. Xing, Q. Xue, Z. Yan, S. Zhuo, et al., Critical role of small micropores in high CO_2 uptake, Phys. Chem. Chem. Phys. 15 (2013) 2523–2529.
[16] T. Tooming, T. Thomberg, H. Kurig, A. Jänes, E. Lust, High power density supercapacitors based on the carbon dioxide activated D-glucose derived carbon electrodes and 1-ethyl-3-methylimidazolium tetrafluoroborate ionic liquid, J. Power Sources 280 (2015) 667–677.
[17] C.H. Kim, J.-H. Wee, Y.A. Kim, K. Seung Yang, C.-M. Yang, Tailoring the pore structure of carbon nanofibers for achieving ultrahigh-energy-density supercapacitors using ionic liquids as electrolytes, J. Mater. Chem. 4 (2016) 4763–4770.
[18] H. Wang, Q. Gao, J. Hu, High hydrogen storage capacity of porous carbons prepared by using activated carbon, J. Am. Chem. Soc. 131 (2009) 7016–7022.
[19] P. Cheng, S. Gao, P. Zang, X. Yang, Y. Bai, H. Xu, et al., Hierarchically porous carbon by activation of shiitake mushroom for capacitive energy storage, Carbon 93 (2015) 315–324.
[20] P. Gong, Z. Wang, J. Wang, H. Wang, Z. Li, Z. Fan, et al., One-pot sonochemical preparation of fluorographene and selective tuning of its fluorine coverage, J. Mater. Chem. 22 (2012) 16950–16956.
[21] H. Itoi, H. Nishihara, T. Kogure, T. Kyotani, Three-dimensionally arrayed and mutually connected 1.2-nm nanopores for high-performance electric double layer capacitor, J. Am. Soc. Chem. 133 (2011) 1165–1167.
[22] Z. Yang, Y. Xia, X. Sun, R. Mokaya, Preparation and hydrogen storage properties of zeolite-templated carbon materials nanocast via chemical vapor deposition: effect of the zeolite template and nitrogen doping, J. Phys. Chem. B 110 (2006) 18424–18431.
[23] M. Sevilla, A.B. Fuertes, Sustainable porous carbons with a superior performance for CO_2 capture, Energy Environ. Sci. 4 (2011) 1765–1771.
[24] E. Raymundo-Pinero, P. Azais, T. Cacciaguerra, D. Cazorla-Amorós, A. Linares-Solano, F. Béguin, KOH and NaOH activation mechanisms of multiwalled carbon nanotubes with different structural organisation, Carbon 43 (2005) 786–795.
[25] C. Long, X. Chen, L. Jiang, L. Zhi, Z. Fan, Porous layer-stacking carbon derived from in-built template in biomass for high volumetric performance supercapacitors, Nano Energy 12 (2015) 141–151.
[26] H.P. Boehm, Some aspects of the surface chemistry of carbon blacks and other carbons, Carbon 32 (1994) 759–769.
[27] J. Moellmer, E.B. Celer, R. Luebke, A.J. Cairns, R. Staudt, M. Eddaoudi, et al., Insights on adsorption characterization of metal-organic frameworks: a benchmark study on the novel soc-MOF, Microporous Mesoporous Mater. 129 (2010) 345–353.
[28] P.I. Ravikovitch, A.V. Neimark, Characterization of micro- and mesoporosity in SBA-15 materials from adsorption data by the NLDFT method, J. Phys. Chem. B 105 (2001) 6817–6823.
[29] A.V. Neimark, P.I. Ravikovitch, Capillary condensation in MMS and pore structure characterization, Microporous Mesoporous Mater. 44 (2001) 697–707.
[30] F. Kleitz, F. Bérubé, R. Guillet-Nicolas, C.-M. Yang, M. Thommes, Probing adsorption, pore condensation, and hysteresis behavior of pure fluids in three-dimensional cubic mesoporous KIT-6 silica, J. Phys. Chem. C 114 (2010) 9344–9355.
[31] Y. Liu, J. Wilcox, Effects of surface heterogeneity on the adsorption of CO_2 in microporous carbons, Environ. Sci. Technol. 46 (2012) 1940–1947.
[32] J.J. Potoff, J.I. Siepmann, Vapor-liquid equilibria of mixtures containing alkanes, carbon dioxide, and nitrogen, AIChE J. 47 (2001) 1676–1682.
[33] D. Dubbeldam, S. Calero, D.E. Ellis, R.Q. Snurr, RASPA: molecular simulation software for adsorption and diffusion in flexible nanoporous materials, Mol. Simulat. 42 (2016) 81–101.
[34] P.E. Fanning, M.A. Vannice, A DRIFTS study of the formation of surface groups on carbon by oxidation, Carbon 31 (1993) 721–730.
[35] Z. Chen, L. Ma, S. Li, J. Geng, Q. Song, J. Liu, et al., Simple approach to carboxyl-rich materials through low-temperature heat treatment of hydrothermal carbon in air, Appl. Surf. Sci. 257 (2011) 8686–8691.
[36] R. Demir-Cakan, N. Baccile, M. Antonietti, M.-M. Titirici, Carboxylate-rich carbonaceous materials via one-step hydrothermal carbonization of glucose

in the presence of acrylic acid, Chem. Mater. 21 (2009) 484–490.
[37] B.M. Kabyemela, T. Adschiri, R.M. Malaluan, K. Arai, Glucose and fructose decomposition in subcritical and supercritical water: detailed reaction pathway, mechanisms, and kinetics, Ind. Eng. Chem. Res. 38 (1999) 2888–2895.
[38] M. Sevilla, A.B. Fuertes, The production of carbon materials by hydrothermal carbonization of cellulose, Carbon 47 (2009) 2281–2289.
[39] T.I.T. Okpalugo, P. Papakonstantinou, H. Murphy, J. McLaughlin, N.M.D. Brown, High resolution XPS characterization of chemical functionalised MWCNTs and SWCNTs, Carbon 43 (2005) 153–161.
[40] W.H. Lee, P.J. Reucroft, Vapor adsorption on coal- and wood-based chemically activated carbons: (I) Surface oxidation states and adsorption of H_2O, Carbon 37 (1999) 7–14.
[41] X. Sun, Y. Li, Colloidal carbon spheres and their core/shell structures with noble-metal nanoparticles, Angew. Chem. Int. Ed. 116 (2004) 607–611.
[42] A. Gęsikiewicz-Puchalska, M. Zgrzebnicki, B. Michalkiewicz, U. Narkiewicz, A.W. Morawski, R.J. Wrobel, Improvement of CO_2 uptake of activated carbons by treatment with mineral acids, Chem. Eng. J. 309 (2017) 159–171.
[43] A. Cuesta, P. Dhamelincourt, J. Laureyns, A. Martinez-Alonso, J.M.D. Tascón, Raman microprobe studies on carbon materials, Carbon 32 (1994) 1523–1532.
[44] V. Chandra, S.U. Yu, S.H. Kim, Y.S. Yoon, D.Y. Kim, A.H. Kwon, et al., Highly selective CO_2 capture on N-doped carbon produced by chemical activation of polypyrrole functionalized graphene sheets, Chem. Commun. 48 (2012) 735–737.
[45] W. Xing, C. Liu, Z. Zhou, L. Zhang, J. Zhou, S. Zhuo, et al., Superior CO_2 uptake of N-doped activated carbon through hydrogen-bonding interaction, Energy Environ. Sci. 5 (2012) 7323–7327.
[46] J. Zhou, Z. Li, W. Xing, T. Zhu, H. Shen, S. Zhuo, N-doped microporous carbons derived from direct carbonization of K^+ exchanged meta-aminophenol-formaldehyde resin for superior CO_2 sorption, Chem. Commun. 51 (2015) 4591–4594.
[47] Z. Liu, Z. Du, H. Song, C. Wang, F. Subhan, W. Xing, et al., The fabrication of porous N-doped carbon from widely available urea formaldehyde resin for carbon dioxide adsorption, J. Colloid Interface Sci. 416 (2014) 124–132.
[48] S. Keskin, T.M. van Heest, D.S. Sholl, Can metal-organic framework materials play a useful role in large-scale carbon dioxide separations? ChemSusChem 3 (2010) 879–891.
[49] K.L. Mulfort, O.K. Farha, C.D. Malliakas, M.G. Kanatzidis, J.T. Hupp, An interpenetrated framework material with hysteretic CO_2 uptake, Chem. Eur J. 16 (2010) 276–281.
[50] J. An, S.J. Geib, N.L. Rosi, High and selective CO_2 uptake in a cobalt adeninate metal-organic framework exhibiting pyrimidine- and amino-decorated pores, J. Am. Chem. Soc. 132 (2009) 38–39.
[51] S.R. Caskey, A.G. Wong-Foy, A.J. Matzger, Dramatic tuning of carbon dioxide uptake via metal substitution in a coordination polymer with cylindrical pores, J. Am. Chem. Soc. 130 (2008) 10870–10871.
[52] N.P. Wickramaratne, M. Jaroniec, Importance of small micropores in CO_2 capture by phenolic resin-based activated carbon spheres, J. Mater. Chem. 1 (2013) 112–116.
[53] J. Rouquerol, F. Rouquerol, P. Llewellyn, G. Maurin, K.S. Sing, Adsorption by Powders and Porous Solids: Principles, Methodology and Applications, Academic press, 2013.
[54] M. Sevilla, C. Falco, M.-M. Titirici, A.B. Fuertes, High-performance CO_2 sorbents from algae, RSC Adv. 2 (2012) 12792–12797.
[55] Y. Xia, R. Mokaya, G.S. Walker, Y. Zhu, Superior CO_2 adsorption capacity on N-doped, high-surface-area, microporous carbons templated from zeolite, Adv. Energy Mater 1 (2011) 678–683.
[56] D. Qian, C. Lei, E.-M. Wang, W.-C. Li, A.-H. Lu, A method for creating microporous carbon materials with excellent CO_2-adsorption capacity and selectivity, ChemSusChem 7 (2014) 291–298.